



# Defect-rich low-crystalline Rh metallene for efficient chlorine-free H<sub>2</sub> production by hydrazine-assisted seawater splitting

Kai Deng, Qiqi Mao, Wenxin Wang, Peng Wang, Ziqiang Wang, You Xu, Xiaonian Li, Hongjing Wang\*, Liang Wang\*

*State Key Laboratory Breeding Base of Green-Chemical Synthesis Technology, College of Chemical Engineering, Zhejiang University of Technology, Hangzhou 310014, PR China*



## ARTICLE INFO

**Keywords:**  
Rh metallene  
Low crystallinity  
Defects  
Seawater splitting  
Hydrazine oxidation reaction

## ABSTRACT

Seawater splitting is considered as a promising way to replace water splitting for H<sub>2</sub> production due to the enrichment of seawater resources. However, the development of this technology has been greatly hampered by the lack of efficient electrocatalysts and the detrimental effects of chlorine electrochemistry. Herein, we report a defect-rich low-crystalline Rh metallene (*l*-Rh metallene) with an amorphous/crystalline hetero-phase structure for seawater electrolysis, where chlorine generation is avoided by replacing the oxygen evolution reaction (OER) with the hydrazine oxidation reaction (HzOR). Benefiting from the large surface-to-volume ratio, abundant active sites and unique electronic structure, the *l*-Rh metallene exhibits out-standing catalytic activity for both hydrogen evolution reaction (HER, -38 mV at 10 mA cm<sup>-2</sup>) and HzOR (-2 mV at 10 mA cm<sup>-2</sup>). Notably, an ultra-low voltage of only 28 mV is required to achieve 10 mA cm<sup>-2</sup> in two-electrode hydrazine-assisted seawater splitting system.

## 1. Introduction

H<sub>2</sub>, as an energy carrier with high energy density and zero emissions, is considered as a sustainable energy alternative to face the over-consumption of fossil fuels [1–4]. Among the various strategies for H<sub>2</sub> production, water splitting is deemed as the most suitable and effective technique [5–9]. Due to the abundance of seawater reserves, direct electrolysis of seawater would be a sustainable strategy to replace water splitting to produce H<sub>2</sub> [10–12]. Nevertheless, two major bottlenecks severely impede the development of direct electrolysis of seawater: (1) the sluggish kinetics for the anodic four-electron oxygen evolution reaction (OER, 4OH<sup>-</sup> → O<sub>2</sub> + 2 H<sub>2</sub>O + 4e<sup>-</sup>) in alkaline media and (2) the competition between the OER and chlorine evolution reaction (CER, Cl<sup>-</sup> + 2OH<sup>-</sup> → ClO<sup>-</sup> + H<sub>2</sub>O + 2e<sup>-</sup>) and corrosion effects induced by the presence of high concentrations of chloride anions [13–15]. Two approaches have been explored for breaking the above bottlenecks. The first is to drastically accelerate the anodic reaction kinetics by replacing the OER with a thermodynamically more favorable electro-oxidation reaction, such as the hydrazine oxidation reaction (HzOR, N<sub>2</sub>H<sub>4</sub> + 4OH<sup>-</sup> → N<sub>2</sub> + 4 H<sub>2</sub>O + 4e<sup>-</sup>) [16–18]. The HzOR possesses a theoretical oxidation potential of -0.33 V (vs. RHE), which is far lower than that of

OER (1.23 V vs. RHE) and CER (2.05 V vs. RHE) [19,20]. The second is the development of efficient and corrosion-resistant electrocatalysts to overcome the impairment of chlorine electrochemistry during the seawater splitting [21,22].

Rh, a Pt-group element, exhibits high activity towards hydrogen evolution reaction (HER) thanks to its physicochemical properties resembling those of Pt [23,24]. In particular, Rh metal has intrinsic high-resistance to corrosion for various electrolyte, making it a potential candidate electrocatalyst for seawater splitting [25,26]. Given the scarcity and high price of the precious metal Rh, structural engineering is a material optimization strategy to boost the catalytic activity and elevate the atom utilization efficiency [27]. Recently, a class of graphene-like two-dimensional (2D) metallic materials called “metallene”, such as Pd [28], PdMo [29] and RhPdH [30] metallene, has generated tremendous enthusiasm among researchers. Compared to their bulk counterparts, these metallene materials have an ultra-high specific surface area and unique electronic structure characteristics that endow them with excellent catalytic properties [31,32]. Zheng’s group reported a CO-confined growth strategy for the preparation of freestanding 2D ultrathin Rh nanosheets [33]. The preferential strong adsorption of CO on the Rh (111) surface plays a key role in the

\* Corresponding authors.

E-mail addresses: [hjw@zjut.edu.cn](mailto:hjw@zjut.edu.cn) (H. Wang), [wangliang@zjut.edu.cn](mailto:wangliang@zjut.edu.cn) (L. Wang).

controlled synthesis of ultrathin 2D structures. Moreover, phase engineering is generally used to improve the electrocatalytic activity of 2D materials through tune their physicochemical properties [34,35]. In particular, 2D hetero-phase nanostructures composed of amorphous and crystalline phases has exhibited some distinct properties and potential catalytic performances owing to the synergistic effect between different phases and the existence of phase boundaries [36]. Zhang's group has synthesized a series of amorphous/crystalline hetero-phase nanomaterials in which the crystallinity can be tuned by controlling the reaction temperature and time [37,38]. As a means to further improve the electronic properties and performance of such 2D hetero-phase nanostructures, researchers are increasingly focusing on defect engineering, involving the construction of defects such as vacancy defects, dislocations and grain boundaries [39]. Through defect engineering, the electronic structure of nanomaterials can be greatly altered to achieve dramatic improvements in electrical conductivity, leading to significant enhancements in catalytic and electrocatalytic properties [40].

Inspired by the above advances, we report a CO-confined growth strategy to synthesize low-crystalline Rh metallene (denoted as *l*-Rh metallene) with defect-rich, ultrathin, layered, highly curved and hetero-phase features. Compared to crystalline Rh metallene (denoted as *c*-Rh metallene) and commercial Pt/C catalysts, the *l*-Rh metallene shows outstanding HER activity and stability for seawater splitting. Furthermore, when combined with HzOR, the *l*-Rh metallene||*l*-Rh metallene two-electrode system exhibits efficient H<sub>2</sub> production in alkaline seawater, while avoiding the chlorine electrochemistry.

## 2. Experimental section

### 2.1. Materials and chemicals

Rhodium(III) acetylacetone (Rh(acac)<sub>3</sub>, 97%) and Nafion (5%) were obtained from Sigma-Aldrich. Rhodium chloride (RhCl<sub>3</sub>, 98%), Rhodium(II) acetate dimer (C<sub>8</sub>H<sub>12</sub>O<sub>8</sub>Rh<sub>2</sub>, Rh: 43.0%–46.6%), oleylamine (OAm, C18: 80–90%), ethylene glycol (EG, 99%), 1-Methyl-2-pyrrolidone (NMP, > 99%), potassium hydroxide (KOH, 85%), borane dimethylamine complex (DMAB, 96%), citrate (CA, ≥99.5%), ascorbic acid (AA, >99%), graphene oxide (GO, >99%), 2-propanol (IPA, ≥99.5%), hydrazine monohydrate (N<sub>2</sub>H<sub>4</sub>·H<sub>2</sub>O, 80%), o-tolidine (98%), and sodium hypochlorite solution (NaClO, 6–14%) were purchased from Shanghai Aladdin Biochemical Technology Co., Ltd. (Shanghai, China). Commercial Pt/C (20 wt%) was ordered from Alfa Aesar. Carbon monoxide (CO, 99.98%) was purchased from Hangzhou Jingong Special Gas Co., Ltd. (Hangzhou, China). The seawater used in this work was collected from the Yellow Sea (Qingdao, China). All the chemicals were used without further purification.

### 2.2. Synthesis of defect-rich low-crystalline Rh metallene (*l*-Rh metallene)

In a typical synthesis of *l*-Rh metallene, 10.3 mg of Rh(acac)<sub>3</sub> and 40 mg of AA were added into a 15 mL glass vial containing 5 mL of OAm. Then, the mixture was heated to 85 °C and stirred for 60 min to get a homogeneous mixture. After that, CO gas was introduced at a flow rate of 200 mL min<sup>-1</sup> for 15 min, then heated to 180 °C and maintained for 90 min. After being cooled to room temperature, the final product was washed and collected with cyclohexane and ethanol for several times, by centrifugation at 10,000 rpm for 5 min. The crystalline Rh metallene (*c*-Rh metallene) were obtained under the same reaction conditions as the *l*-Rh metallene except that the reaction time was changed to 12 h.

### 2.3. Characterizations

The morphology and structure of the prepared materials were characterized by transmission electron microscopy (TEM, JEM-2100 F, JEOL, Japan) at 200 kV and atomic force microscopy (AFM, MFP-3D Infinity, Asylum Research, the US) respectively. In addition, high-

angle annular dark field-scanning transmission electron microscope (HAADF-STEM), high-resolution TEM (HR-TEM), selected area electron diffraction (SEAD), and element mapping analysis tests were also performed on TEM. The physical surface area was calculated from the Brunauer-Emmett-Teller isotherm (BET, Autosorb-IQ3, Quantachrome, the US). The crystalline phase and surface electronic structure of the catalysts were analyzed by X-ray powder diffraction (XRD, Ultima IV, Rigaku, Japan) and X-ray photoelectron spectroscopy (XPS, K-Alpha, Thermo Scientific, the US), respectively. Ultraviolet-visible (UV-vis) spectra were recorded at room temperature on a TU-1900 spectrophotometer (PERSEE, China) equipped with 1.0 cm quartz cells.

### 2.4. Electrochemical experiments

CHI 760E electrochemical workstation (CHI Instruments, China) was used to test the half-cell HzOR and HER performance in a three-electrode system, in which a catalyst-coated glassy carbon electrode (GCE), Hg/HgO (1.0 M KOH) and a graphite rod were used as the working, reference and counter electrodes, respectively. For the preparation of the working electrode, 2 mg of the prepared *l*-Rh metallene was first mixed with 720 μL of deionized water, 200 μL of 2-propanol and 80 μL of Nafion, and then the mixture was sonicated for 60 min and dropped on polished GCE with a loading content of 6 μg. The *c*-Rh metallene and commercial Pt/C catalysts was also prepared using the same procedure and tested as a comparison samples. All potentials in polarization curves were obtained with iR compensation using the equation:  $E(iR\text{-compensated}) = E - iR$ , where *i* is the current and *R* is the uncompensated electrolyte ohmic resistance measured by electrochemical impedance spectroscopy. In this work, all potentials were converted to the reversible hydrogen electrode (RHE). For the HER test, linear sweep voltammetry (LSV) curves were conducted in a 1 M KOH seawater electrolyte at a scan rate of 5 mV s<sup>-1</sup>. For the HzOR test, LSV curves were acquired in a 1 M KOH seawater electrolyte containing 0.1 M N<sub>2</sub>H<sub>4</sub> at a scan rate of 5 mV s<sup>-1</sup>. The HER||HzOR system was carried out in a homemade two-electrode mode with the *l*-Rh metallene as the anode and cathode electrode material. For the preparation of the working electrode, 5 mg of the prepared *l*-Rh metallene was first mixed with 1 mL of a solution containing 720 μL of deionized water, 200 μL of 2-propanol and 80 μL of Nafion, and then the mixture was sonicated for 60 min and dropped on carbon paper (1 × 1 cm) with a loading content of 1 mg cm<sup>-2</sup>. The polarization curves were measured at a scan rate of 5 mV s<sup>-1</sup> in a 1 M KOH seawater electrolyte containing 0.1 M N<sub>2</sub>H<sub>4</sub>. The amounts of Cl<sub>2</sub> can be test during the seawater splitting due to its high solubility in water (Cl<sub>2</sub> + H<sub>2</sub>O ⇌ HCl + HClO), in which the HClO can be detected by o-tolidine test. The test solution contains 10 mL of Deionized (DI) water and 0.5 mL of o-tolidine solution (0.05 M in ethanol).

## 3. Results and discussion

### 3.1. Synthesis and characterization of *l*-Rh metallene

The schematic illustration of the preparation process of *l*-Rh metallene is displayed in Fig. 1a. The *l*-Rh metallene is synthesized through a CO-confined growth strategy using Rh(acac)<sub>3</sub> as the precursor, AA as the reductant, OAm as the solvent and surfactant, and CO as the surface confining agent. Low- and high-magnification HAADF-STEM and TEM images of *l*-Rh metallene exhibit a typical 2D structure with high yields, which is analogous with that of graphene oxide (Fig. 1b-e, Fig. S1 and Fig. S2). The obtained *l*-Rh metallene exhibits a wrinkled structure with a continuous distribution of lateral dimensions exceeding 2.0 μm. Fig. 1f shows that *l*-Rh metallene architecture is constructed by several overlapping nanosheets and the interlayer spacing of those nanosheets is measured to be about 2.0 nm. The ultrathin character of *l*-Rh metallene is demonstrated by TEM and AFM. The monolayer nanosheet is translucent to the electron beam and numerous pores appeared after high-magnification TEM measurements, indicative of its ultra-thin nature

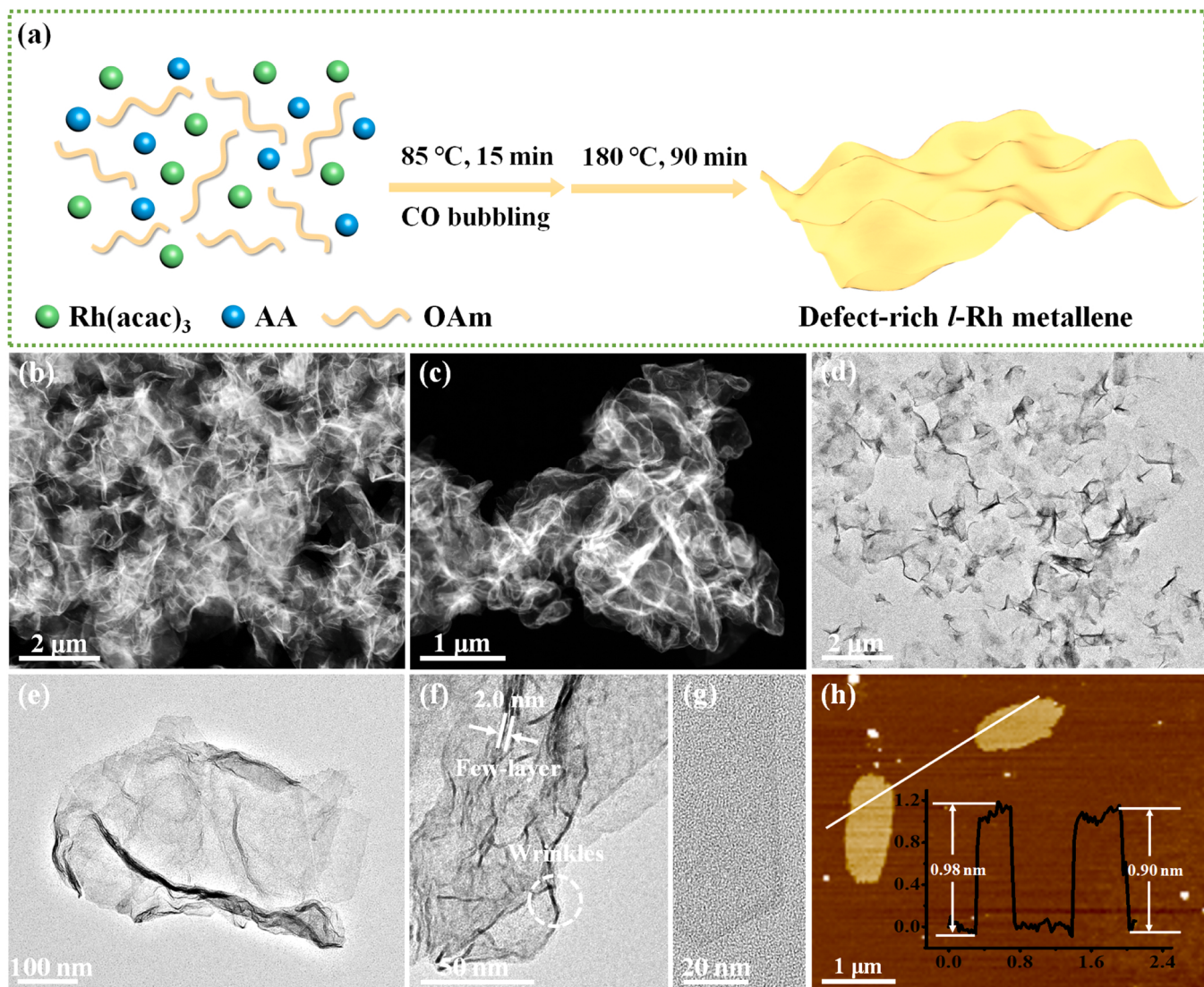


**Fig. 1.** (a) Schematic illustration of the synthesis process of *l*-Rh metallene. (b and c) low- and high-magnification HAADF-STEM, (d-g) low- and high-magnification TEM and (h) AFM images of *l*-Rh metallene. The inset in (h) is the corresponding height profiles of *l*-Rh metallene.

(Fig. 1g and Fig. S3). The thickness of the nanosheets is less than 1 nm, equivalent to about 5 at. layers, which further confirms their ultrathin nature (Fig. 1h). Based on the N<sub>2</sub> adsorption-desorption isotherm date (Fig. S4), the BET surface area of *l*-Rh metallene is calculated to be 43.61 m<sup>2</sup> g<sup>-1</sup>. Such a large specific surface area of *l*-Rh metallene materials will motivates their use in surface-active catalytic reactions. Moreover, the unique 2D nanosheets with ultrathin multilayer configurations enable electron confinement and provide rich interlayer channels, which guarantee faster interfacial charge transfer and facilitate mass transfer, favoring the electrocatalytic processes. The presence of Rh elements in *l*-Rh metallene is confirmed by STEM elemental mapping analysis (Fig. S5). The c-Rh metallene can be prepared by controlling the reaction temperature. HAADF-STEM, TEM, HRTEM and XRD show that the obtained c-Rh metallene exhibits an ordered 2D nanosheet structure with a high degree of crystalline properties (Fig. S6).

To investigate *l*-Rh metallene at the atomic scale, HRTEM is performed. As shown in Fig. 2a and Fig. 2b, a typical *l*-Rh metallene possesses many amorphous domains and the boundary of the amorphous/crystalline phase can be clearly observed. The SAED pattern shows no obvious diffusion ring, verifying the low crystallinity nature of the amorphous/crystalline hetero-phase *l*-Rh metallene (Fig. 2c). In the representative crystalline region (I), the Rh atoms are well-ordered and

the spacing of the lattice fringes is 0.22 nm, corresponding to the face centered cubic (fcc) Rh (111) crystal plane, while in the representative amorphous region (II), the atoms are randomly arranged and exhibit numerous lattice disorders. The corresponding fast Fourier transform (FFT) patterns of the selected regions show bright spots and diffuse rings, which further demonstrate the crystalline and amorphous phases in the *l*-Rh metallene (Fig. 2d and Fig. 2e). Detailed HRTEM images show the nature of its crystalline parts with abundant atomic defects, grain boundaries and twin boundaries (Fig. 2f and Fig. 2g). Such a special crystal structure not only regulates its electronic structure but also provides additional catalytic active sites, which facilitates the improvement of electrocatalytic activity. The XRD pattern of *l*-Rh metallene shows weak diffraction peaks (Fig. 2h), suggesting its poor crystallinity, which is consistent with the results of HRTEM and SAED. The amorphous phase with a large number of lattice disorders can provide abundant active sites, while its structural flexibility can facilitate charge and electron diffusion, thus promoting electrocatalytic performance. The chemical state of Rh is investigated by XPS. From the XPS spectra (Fig. 2i), the binding energy (BE) of *l*-Rh metallene located at 308.0 and 312.65 eV can be assigned to 3d<sub>5/2</sub> and 3d<sub>3/2</sub> of metallic Rh, respectively. Compared to the standard BE values of 307.0 eV (3d<sub>5/2</sub>) and 311.75 eV (3d<sub>3/2</sub>) for Rh 3d, the values for *l*-Rh metallene show a

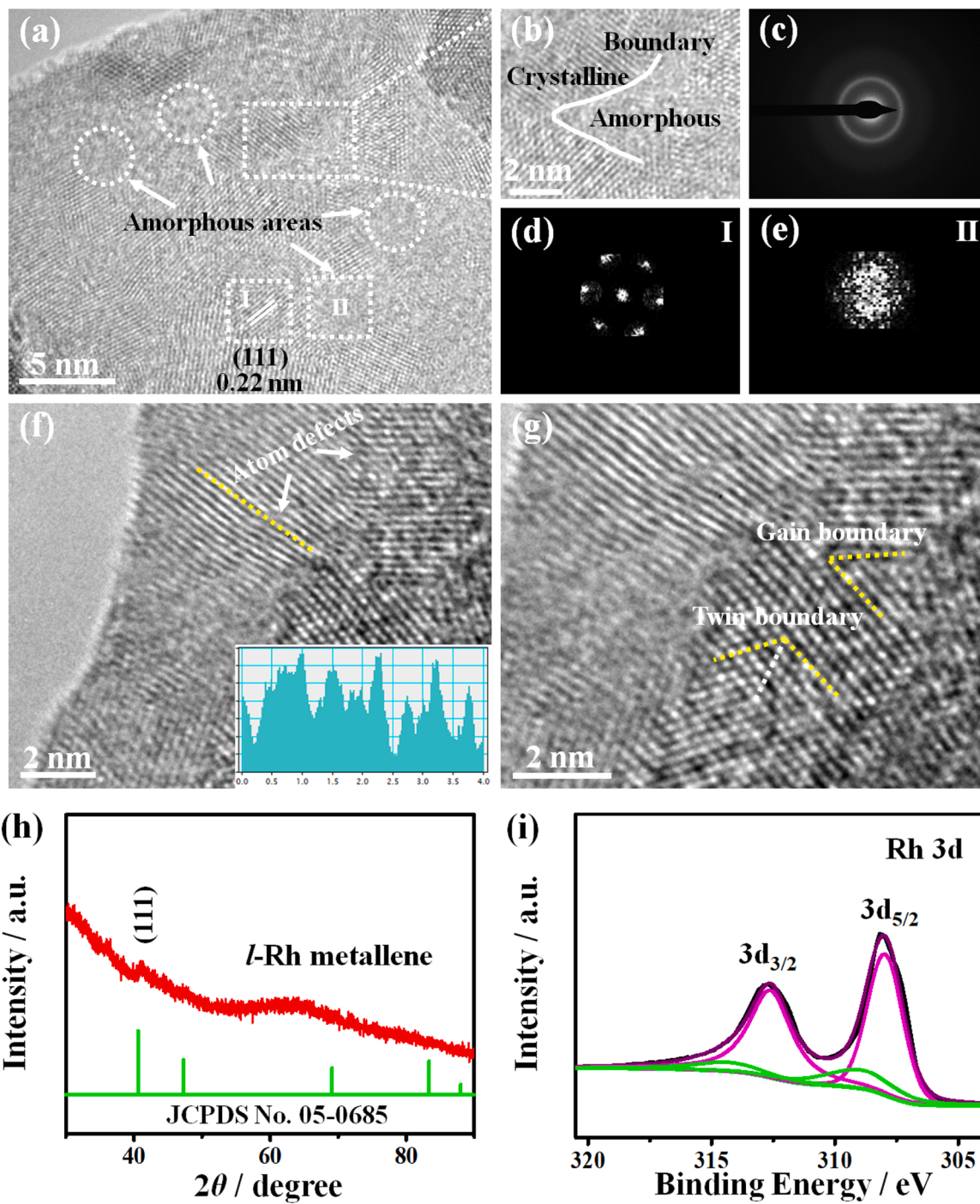


**Fig. 2.** (a) HRTEM image, (b) enlarged HRTEM image of the selected area and (c) SAED pattern of *l*-Rh metallene. (d and e) The corresponding FFT patterns of the selected areas I and II in (a). (f and g) HRTEM images of *l*-Rh metallene. (h and i) XRD pattern and Rh 3d XPS spectrum of *l*-Rh metallene. The inset in (f) is the intensity profile along the line.

pronounced shift to higher BE, which may be attributed to the particularly electronic structure of hetero-phase ultrathin 2D nanosheets [41].

To clarify the formation mechanism of *l*-Rh metallene, a series of control experiments are carried out. The time-dependent experiments are first investigated to trap the shape evolution of *l*-Rh metallene with reaction time. The products obtained at early stage of the reaction (45 min) exhibit a typical curved 2D nanosheets structure (Fig. S7a and Fig. S7b). As the reaction continues, the nanosheets show a growth trend of increasing lateral size and prominent wrinkled features, eventually forming high-quality graphene-like structures (Fig. S7c and Fig. S7d). The morphology of the nanosheets will not further evolve despite the

extension of the reaction time to 90 min. The results suggest that the nanosheets are most likely fabricated directly from the precursors under a controlled experimental condition. As demonstrated in previous reports [33], the presence of CO plays a crucial role in inducing the growth of ultrathin 2D Rh nanosheets. In the absence of CO, only nonuniform Rh agglomerates consisting of small particles are obtained (Fig. S8). To reveal the interactions between CO and Rh, CO stripping voltammogram of the freshly prepared *l*-Rh metallene is investigated. From the CO stripping curve, the peak can be assigned to the CO adsorption on the (111) facets of the as-prepared Rh nanosheets (Fig. S9). Then, the roles of the other reaction parameters (including AA, solvents, and

precursors) were further investigated. If no AA is added, the as-prepared product exhibits a poor quality nanosheet morphology with extensive Rh nanoparticles attached (Fig. S10a and Fig. S10b). When the amount of AA is 80 mg, the morphology of the nanosheets became highly curved (Fig. S10c and Fig. S10d). As the amount of AA is increased to 160 mg, most of the nanosheets disappeared and tended to form agglomerates due to the rapid reduction kinetics of the system derived from the large amount of reducing agent (Fig. S10e and Fig. S10f). But when AA is replaced by DMAB and CA, high quality nanosheets could not be synthesized (Fig. S11). The selection of Rh(acac)<sub>3</sub> as precursor is also crucial for the formation of well-shaped *l*-Rh metallene in our system. Using C<sub>8</sub>H<sub>12</sub>O<sub>8</sub>Rh<sub>2</sub> and RhCl<sub>3</sub> as precursors, a mixture of Rh nanosheets and nanoflower or nanoparticles is produced (Fig. S12). OAm as an effective stabilizer is the key to prepare highly dispersed nanosheet. When only OAm are involved, many small Rh nanoparticles with good monodispersed can still be produced (Fig. S13). Instead, the severely agglomerated Rh nanostructure formed if NMP and EG is used (Fig. S14). These results confirm the key role of CO, AA, OAm and Rh (acac)<sub>3</sub> in the formation of *l*-Rh metallene. Our approach can also be extended to scale-up (10 times) synthesis of *l*-Rh metallene (Fig. S15).

### 3.2. Electrocatalytic performances for HER

The electrocatalytic HER performance of *l*-Rh metallene, *c*-Rh metallene and Pt/C catalysts is evaluated in a 1.0 M KOH seawater electrolyte by using a typical three-electrode system. Fig. 3a compares the LSV curves of *l*-Rh metallene, *c*-Rh metallene and Pt/C. It only requires a low overpotential of 38 mV to achieve a current density of 10 mA cm<sup>-2</sup> for *l*-Rh metallene, which is much lower than *c*-Rh metallene (49 mV) and benchmark Pt/C (47 mV) (Fig. 3b). The corresponding Tafel slope is calculated to be 39.0 mV dec<sup>-1</sup> (Fig. 3c), which is smaller than the value of the benchmark Pt/C and close to the theoretical value (~40 mV dec<sup>-1</sup>) in alkaline electrolyte [42], indicating that the HER process on *l*-Rh metallene undergoes a fast Volmer-Heyrovsky pathway. Besides the Tafel slope, the exchange current density ( $J_0$ ) is also investigated to further assess the intrinsic specific activity. The calculated  $J_0$  for *l*-Rh

metallene is 1.04 mA cm<sup>-2</sup>, which is larger than that of Pt/C (1.03 mA cm<sup>-2</sup>), revealing a higher intrinsic electron-transfer rates between *l*-Rh metallene and the electrolyte. The electrochemically active surface area (ECSA) is collected, which is linearly proportional to the value of the double-layer capacitance ( $C_{dl}$ ) derived from the CV curves (Fig. S16). The values of  $C_{dl}$  are calculated to be 3.45, 3.22 and 3.33 mF cm<sup>-2</sup> for *l*-Rh metallene, *c*-Rh metallene and Pt/C, respectively, implying more accessible active sites owned by *l*-Rh metallene (Fig. 3d). Turnover frequency (TOF) is also an important criterion for evaluating HER activity, and it is calculated based on previous reports [43]. The TOF value of *l*-Rh metallene is 1.41 s<sup>-1</sup> at 100 mV, which is higher than that of *c*-Rh metallene (0.92 s<sup>-1</sup>), indicating its excellent HER catalytic activity. To better understand the interfacial charge transfer kinetics, Nyquist plots are obtained from electrochemical impedance spectroscopy (EIS) measurements (Fig. S17a), where *l*-Rh metallene possesses the smallest semicircle corresponds to the smallest charge transfer resistance ( $R_{ct}$ ). The calculated  $R_{ct}$  of *l*-Rh metallene (38.78 Ω) is lower than that of *c*-Rh metallene (54.67 Ω) and Pt/C (48.22 Ω), indicating a faster electron transfer within the *l*-Rh metallene catalyst during the HER process. To further investigate the nature of charge transfer, the typical I-V curves of *l*-Rh metallene and *c*-Rh metallene are observed (Fig. S17b). The non-linear behavior of these curves clearly indicates that *l*-Rh metallene retains its metallic property even with an amorphous/crystalline hetero-phase structure [44]. Being one of the key factors for practical applications, the durability of *l*-Rh metallene is subsequently evaluated. The LSV curves of *l*-Rh metallene exhibits little change between the initial and after 10,000 cycles (Fig. 3e). In addition, the chronoamperometric test is also applied, where the current density could be maintained at 10 mA cm<sup>-2</sup> for 20 h without significant decay (Fig. 3f). From the combined results of the CV and chronoamperometric tests, the outstanding long-term stability of *l*-Rh metallene towards HER can be proved.

### 3.3. Electrocatalytic performances for HzOR

The electrocatalytic performance of *l*-Rh metallene, *c*-Rh metallene

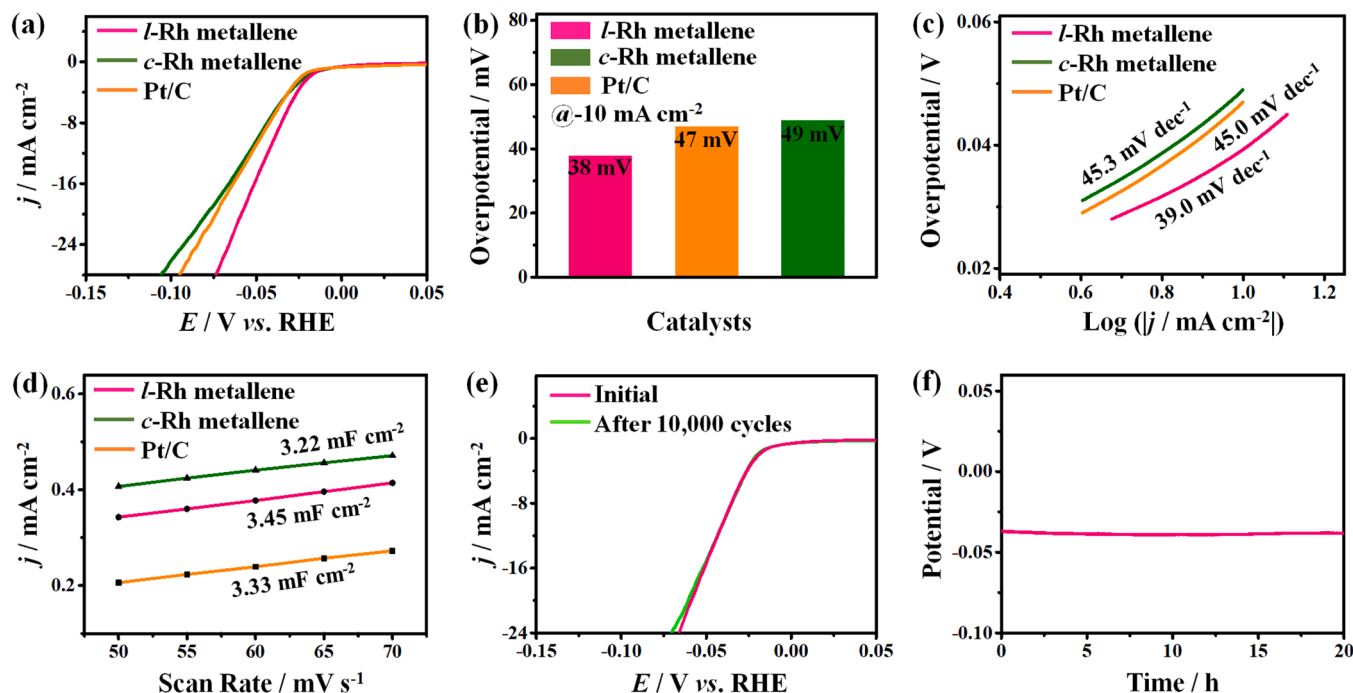


**Fig. 3.** Electrocatalytic HER performance of *l*-Rh metallene, *c*-Rh metallene and Pt/C in alkaline seawater electrolyte. (a) polarization curves, (b) overpotentials at  $-10 \text{ mA cm}^{-2}$ , (c) Tafel slopes and (d) double-layer capacitance ( $C_{dl}$ ) plots. (e) Polarization curves of *l*-Rh metallene before and after 10,000 CV cycles. (f) The chronopotentiometry test recorded at  $10 \text{ mA cm}^{-2}$  for 20 h.

and Pt/C catalysts for HzOR is further evaluated in an electrolyte containing 1.0 M KOH seawater with 0.1 M N<sub>2</sub>H<sub>4</sub> by assembling a typical three-electrode system. The LSV curves of *l*-Rh metallene, *c*-Rh metallene and Pt/C are displayed in Fig. 4a. It can be seen that the *l*-Rh metallene exhibits a superior HzOR activity, and only an ultralow working potential of -2 mV is required to achieve a current density of 10 mA cm<sup>-2</sup>, which is far more excellent than that of *c*-Rh metallene (22 mV) and Pt/C (209 mV) (Fig. 4b). Importantly, the electrocatalytic activity of HzOR is significantly better than that of OER (Fig. S18), suggesting that HzOR could be an ideal anodic alternative to replace the OER for seawater splitting. The corresponding Tafel slope of *l*-Rh metallene is much smaller than that of Pt/C (Fig. 4c), which suggests that the HzOR process undergoes more favorable catalytic kinetics on the *l*-Rh metallene electrode. In addition to the electrocatalytic activity, the long-term stability of *l*-Rh metallene towards HzOR is also investigated by chronoamperometry and CV measurements. The LSV curves of *l*-Rh metallene shows negligible decay after 10,000 cycles for HzOR (Fig. 4d). Additionally, the current density displays insignificant potential decay after 20 h continuous HzOR operation at 10 mA cm<sup>-2</sup> (Fig. S19).

#### 3.4. Electrocatalytic performances for low-voltage H<sub>2</sub> production from seawater

Inspired by the excellent performance of *l*-Rh metallene for both HER and HzOR, we further assembled a two-electrode system for energy-saving electrochemical H<sub>2</sub> production based on overall hydrazine splitting (OHzS) using the bifunctional *l*-Rh metallene as both cathode and anode electrode materials in a 1.0 M KOH seawater/0.1 M N<sub>2</sub>H<sub>4</sub> electrolyte (Fig. 5a). In contrast, the overall water splitting (OWS) is also measured in the absence of N<sub>2</sub>H<sub>4</sub>. The LSV curve of OHzS shows an obvious negative shift compared to that of OWS (Fig. 5b), which

suggests that a significant energy efficiency improvement can be achieved with HzOR-assisted H<sub>2</sub> production. Encouragingly, only a cell voltage of 36, 115, 169 and 239 mV are required for the OHzS system to achieve 10, 50, 100 and 200 mA cm<sup>-2</sup> (Fig. 5c), respectively, which is much less than the OWS system (1.35, 1.70, 1.77, and 1.87 V, respectively) to obtain the same current density. The electrocatalytic activity of the hydrazine-assisted H<sub>2</sub> production for the *l*-Rh metallene is better than that of the *c*-Rh metallene (Fig. S20). Moreover, the cell voltage of *l*-Rh metallene is also less than that of the recently reported state-of-the-art catalysts for hydrazine-assisted H<sub>2</sub> production (Table S1). The amount of experimentally generated H<sub>2</sub> is in excellent agreement with the theoretical values (Fig. 5d), indicating that the *l*-Rh metallene||*l*-Rh metallene two-electrode system exhibited highly efficient H<sub>2</sub> production with HzOR-assisted. As a comparison, the Faraday efficiency of H<sub>2</sub> production in the OWS process is nearly 100% (Fig. S21). As to concern over electrode corrosion cause by Cl<sup>-</sup> at a high current density during long-term seawater electrolysis, the catalyst durability is assessed using chronoamperometric test in a 1.0 M KOH seawater/0.1 M N<sub>2</sub>H<sub>4</sub> electrolyte at 100 mA cm<sup>-2</sup> 50 h. Fig. 5e shows the *l*-Rh metallene||*l*-Rh metallene with no obvious current changes over a 50 h period, indicating no evident corrosion effects during H<sub>2</sub> production from hydrazine-assisted seawater splitting process. A detailed post-OHzS characterizations of *l*-Rh metallene are carried out to further understand long-term stability. The unique 2D ultrathin multilayer nanosheet structure could be well retained even in such harsh conditions (Fig. S22a). The STEM elemental mapping is used to confirm the elements in the material after testing. No C element is detected after the reaction indicating that the surface adsorbed CO is not present anymore (Fig. S22b), and no carbon deposit is generated during the whole electrochemical test. XRD and XPS are performed to further reveal the crystal structure and chemical state of *l*-Rh metallene after long-term

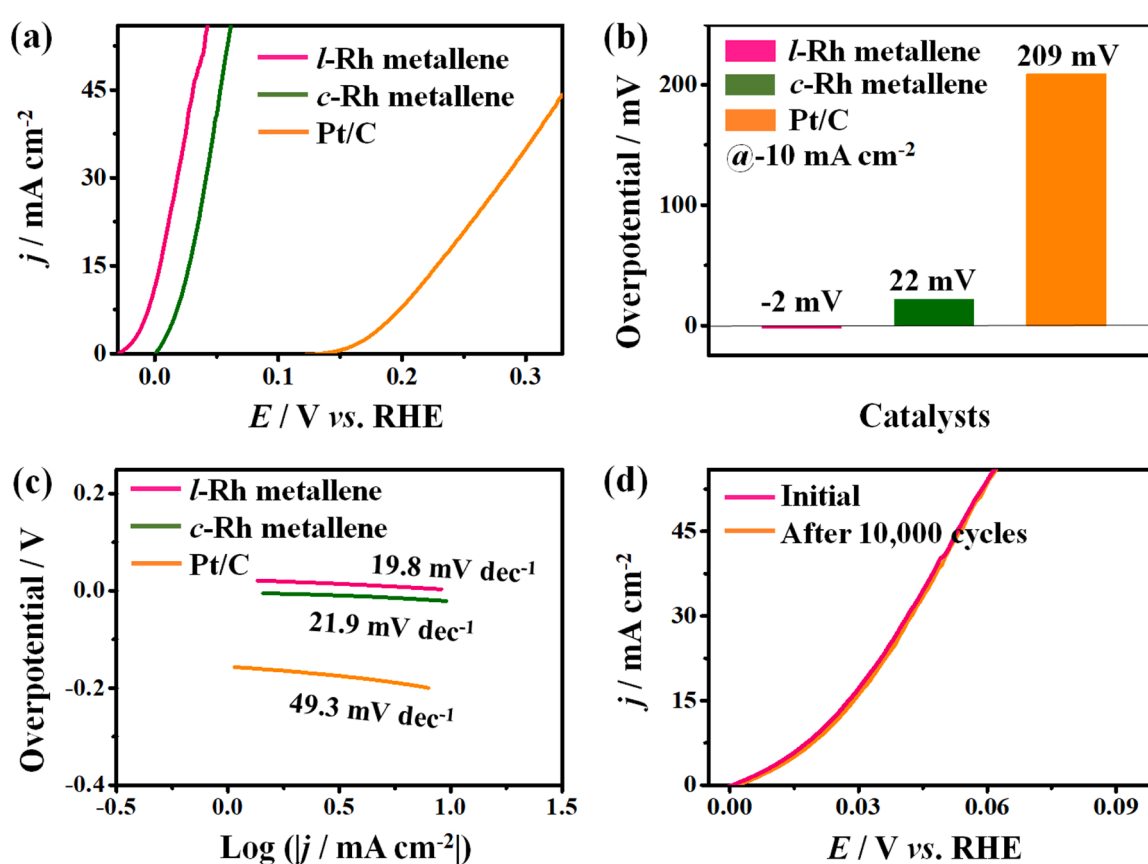
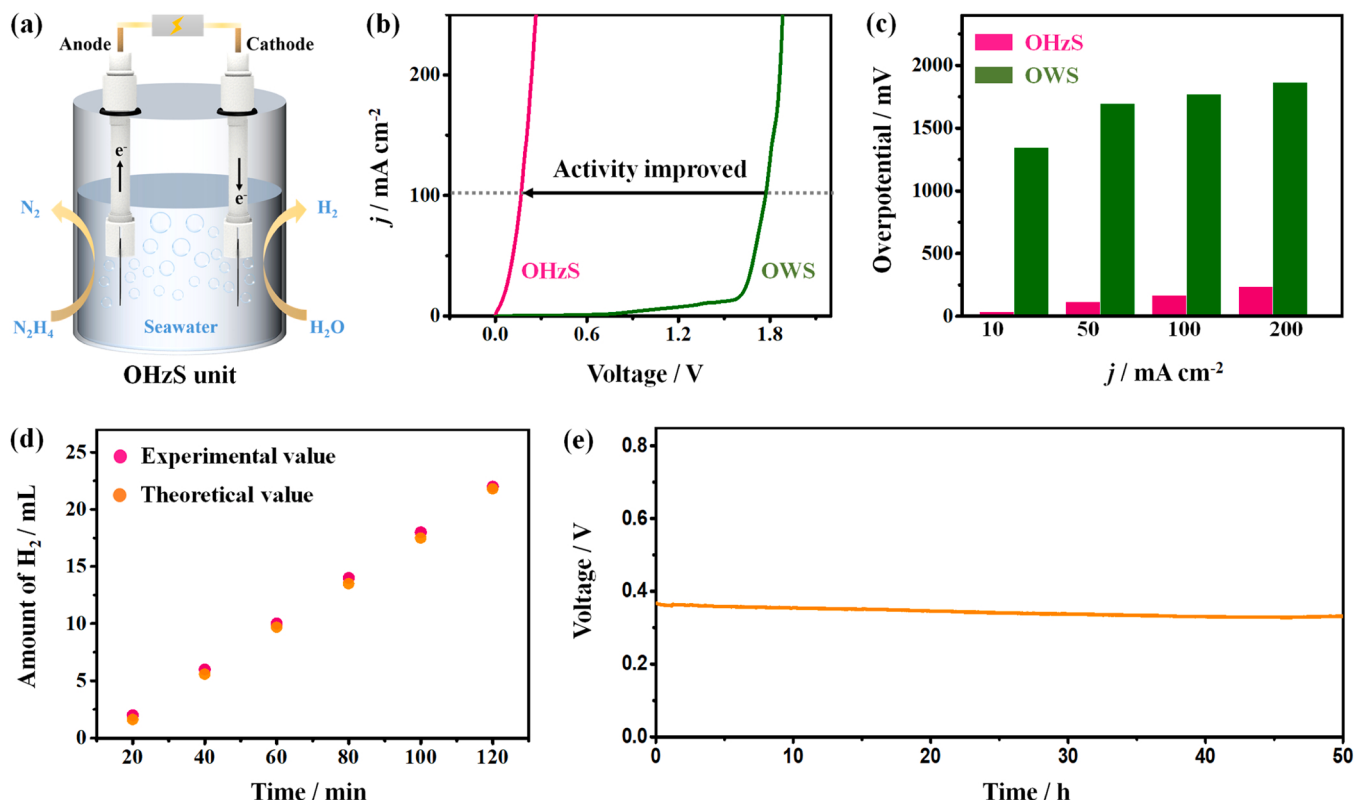


Fig. 4. Electrocatalytic activity towards HzOR in alkaline seawater/0.1 M N<sub>2</sub>H<sub>4</sub> electrolyte. (a) polarization curves, (b) Tafel slopes and (c) overpotentials at -10 mA cm<sup>-2</sup>. (d) Polarization curves of *l*-Rh metallene before and after 10,000 CV cycles.



**Fig. 5.** (a) Schematic illustration for two-electrode hydrazine-assisted seawater splitting system. (b) Comparison of LSV curves for OHzS in alkaline seawater/ $0.1 \text{ M N}_2\text{H}_4$  and OWS in alkaline seawater using *l*-Rh metallene as both the anode and cathode. (c) Comparison of the overpotentials required to reach different current densities for OHzS and OWS. (d) The amount of  $\text{H}_2$  theoretically calculated and experimental measured for OHzS. (e) The chronopotentiometry test for OHzS recorded at  $100 \text{ mA cm}^{-2}$  for 50 h.

durability testing. The *l*-Rh metallene still maintains a low crystal structure (Fig. S22c), further revealing its robust durability. There is an increase in O content from the XPS data, which is attributed to the oxidation of the sample at the anode during the test (Fig. S22d). In addition to corrosion effects, possible chloride oxidation is another key factor in reducing the efficiency of direct electrolysis of seawater. The presence of a liquid phase chloride oxidation product ( $\text{HClO}/\text{ClO}^-$ ) after continuous seawater electrolysis is examined using an *o*-tolidine test. No  $\text{HClO}$  or  $\text{ClO}^-$  formation is observed in the *o*-tolidine test (Fig. S23). These results show that *l*-Rh metallene not only exhibit excellent corrosion resistance, but also present efficient  $\text{H}_2$  production while avoiding the chlorine evolution.

The efficient  $\text{H}_2$  production performance from alkaline seawater splitting can be attributed to the following advantages: (I) The unique 2D ultrathin nanosheets structure of *l*-Rh metallene could provide abundant electrochemical active sites, favoring the electrocatalytic processes. (II) The amorphous/crystalline hetero-phase structure possesses numerous lattice disorders and grain boundaries, which can provide abundant active sites and edge catalytic sites. (III) The special electronic structure of the hetero-phase *l*-Rh metallene guarantees excellent electron transfer capability, thus promoting electrocatalytic performance. (IV) Replacing OER with HzOR which is a more thermodynamically favorable electro-oxidation reaction overcomes the sluggish anodic reaction kinetics and the impairment of chlorine electrochemistry during seawater electrolysis, thus enabling energy-saving  $\text{H}_2$  generation.

#### 4. Conclusion

In summary, we have successfully designed a defect-rich low-crystalline Rh metallene with an amorphous/crystalline hetero-phase

structure for efficient chlorine-free  $\text{H}_2$  production by hydrazine-assisted seawater splitting. The unique multilayer 2D ultrathin nanosheets, defect-rich and hetero-phase structure endow *l*-Rh metallene with abundant electrochemical active sites, excellent mass transport/diffusion capability and high electrical conductivity, resulting in excellent HER and HzOR performance. It only requires overpotential of 38 and  $-2 \text{ mV}$  to achieve a current density of  $10 \text{ mA cm}^{-2}$  for the HER and HzOR electrocatalysis. The *l*-Rh metallene||*l*-Rh metallene two-electrode system exhibits enhanced electrocatalytic activity toward OHzS in alkaline seawater, with ultra-low voltage of 28 mV to deliver  $10 \text{ mA cm}^{-2}$ , almost 100% Faraday efficiency, as well as excellent long-term catalytic durability. This work not only demonstrates that *l*-Rh metallene is an efficient catalyst for HER and HzOR, but also may provide a powerful strategy for efficient  $\text{H}_2$ .

#### CRediT authorship contribution statement

**Kai Deng:** Experimental measurements, Data analysis, Manuscript Preparation. **Qiqi Mao:** Experimental measurements, Data analysis. **Wenxin Wang:** Experimental measurements. **Peng Wang:** Data curation. **Ziqiang Wang:** Reviewing and editing. **You Xu:** Conceptualization, Supervision, Funding acquisition. **Xiaonian Li:** Supervision. **Hongjing Wang:** Reviewing and editing, Supervision, Project administration. **Liang Wang:** Reviewing and editing, Supervision, Project administration.

#### Declaration of Competing Interest

The authors declare that they have no known competing financial interests or personal relationships that could have appeared to influence the work reported in this paper.

## Acknowledgement

This work was financially supported by the National Natural Science Foundation of China (No. 21776255, 21972126, 21978264, 21905250).

## Appendix A. Supporting information

Supplementary data associated with this article can be found in the online version at [doi:10.1016/j.apcatb.2022.121338](https://doi.org/10.1016/j.apcatb.2022.121338).

## References

- [1] Y. Yao, Y.H. Zhu, C.A.Q. Pan, C.Y. Wang, S.Y. Hu, W. Xiao, X. Chi, Y.R. Fang, J. Yang, H.T. Deng, S.Q. Xiao, J.B. Li, Z. Luo, Y.B. Guo, Interfacial sp C-O-Mo hybridization originated high-current density hydrogen evolution, *J. Am. Chem. Soc.* 143 (2021) 8720–8730, <https://doi.org/10.1021/jacs.1c02831>.
- [2] J. Zhu, L.S. Hu, P.X. Zhao, L.Y.S. Lee, K.Y. Wong, Recent advances in electrocatalytic hydrogen evolution using nanoparticles, *Chem. Rev.* 120 (2020) 851–918, <https://doi.org/10.1021/cr000248>.
- [3] A.R.P. Santiago, T.W. He, O. Eraso, M.A. Ahsan, A.N. Nair, V.S.N. Chava, T. Zheng, S. Pilla, O. Fernandez-Delgado, A.J. Du, S.T. Sreenivasan, L. Echegoyen, Tailoring the interfacial interactions of van der Waals 1T-MoS<sub>2</sub>/C<sub>60</sub> heterostructures for high-performance hydrogen evolution reaction Electrocatalysis, *J. Am. Chem. Soc.* 142 (2020) 17923–17927, <https://doi.org/10.1021/jacs.0c08867>.
- [4] Z. Wang, B. Xiao, Z. Lin, Y. Xu, Y. Lin, F. Meng, Q. Zhang, L. Gu, B. Fang, S. Guo, W. Zhong, PtSe<sub>2</sub>/Pt heterointerface with reduced coordination for boosted hydrogen evolution reaction, *Angew. Chem. Int. Ed.* 133 (2021) 23576–23581, <https://doi.org/10.1002/anie.202110335>.
- [5] L.G. Li, P.T. Wang, Q. Shao, X.Q. Huang, Metallic nanostructures with low dimensionality for electrochemical water splitting, *Chem. Soc. Rev.* 49 (2020) 3072–3106, <https://doi.org/10.1039/d0cs00013b>.
- [6] W.J. Jiang, T. Tang, Y. Zhang, J.S. Hu, Synergistic modulation of non-precious-metal electrocatalysts for advanced water splitting, *Acc. Chem. Res.* 53 (2020) 1111–1123, <https://doi.org/10.1021/acs.accounts.0c00127>.
- [7] H.M. Wang, Z.N. Chen, D.S. Wu, M.N. Cao, F.F. Sun, H. Zhang, H.H. You, W. Zhuang, R. Cao, Significantly enhanced overall water splitting performance by partial oxidation of Ir through Au modification in core-shell alloy structure, *J. Am. Chem. Soc.* 143 (2021) 4639–4645, <https://doi.org/10.1021/jacs.0c12740>.
- [8] T.T. Zheng, C.Y. Shang, Z.H. He, X.Y. Wang, C. Cao, H.L. Li, R. Si, B.C. Pan, S. M. Zhou, J. Zeng, Intercalated iridium diselenide electrocatalysts for efficient pH-universal water splitting, *Angew. Chem. Int. Ed.* 58 (2019) 14764–14769, <https://doi.org/10.1002/anie.201909369>.
- [9] Q. Yao, B.L. Huang, N. Zhang, M.Z. Sun, Q. Shao, X.Q. Huang, Channel-rich RuCu nanosheets for pH-universal overall water splitting electrocatalysis, *Angew. Chem. Int. Ed.* 58 (2019) 13983–13988, <https://doi.org/10.1002/anie.201908092>.
- [10] D.L. Wu, D. Chen, J.W. Zhu, S.C. Mu, Ultralow Ru incorporated amorphous cobalt-based oxides for high-current-density overall water splitting in alkaline and seawater media, *Small* 17 (2019), 2102777, <https://doi.org/10.1002/smll.202012777>.
- [11] W.J. Zang, T. Sun, T. Yang, S.B. Xi, M. Waqar, Z.K. Kou, Z.Y. Lyu, Y.P. Feng, J. Wang, S.J. Pennycook, Efficient hydrogen evolution of oxidized Ni<sub>3</sub>N defective sites for alkaline freshwater and seawater electrolysis, *Adv. Mater.* 33 (2021), 2003846, <https://doi.org/10.1002/adma.202003846>.
- [12] Y.Q. Zhao, B. Jin, Y. Zheng, H.Y. Jin, Y. Jiao, S.Z. Qiao, Charge state manipulation of cobalt selenide catalyst for overall seawater electrolysis, *Adv. Energy Mater.* 8 (2018), 1801926, <https://doi.org/10.1002/aenm.201801926>.
- [13] H.J. Chen, Y.H. Zou, J. Li, K.W. Zhang, Y.Z. Xia, B. Hui, D.J. Yang, Wood aerogel-derived sandwich-like layered nanoelectrodes for alkaline overall seawater electrosplitting, *Appl. Catal. B-Environ.* 293 (2021), 120215, <https://doi.org/10.1016/j.apcatb.2021.120215>.
- [14] L. Yu, Q. Zhu, S.W. Song, B. McElhenney, D.Z. Wang, C.Z. Wu, Z.J. Qin, J.M. Bao, Y. Yu, S. Chen, Z.F. Ren, Non-noble metal-nitride based electrocatalysts for high-performance alkaline seawater electrolysis, *Nat. Commun.* 10 (2019) 5106, <https://doi.org/10.1038/s41467-019-13092-7>.
- [15] T.F. Ma, W.W. Xu, B.R. Li, X. Chen, J.J. Zhao, S.S. Wan, K. Jiang, S.X. Zhang, Z. F. Wang, Z.Q. Tian, Z.Y. Liu, L. Chen, The critical role of additive sulfate for stable alkaline seawater oxidation on nickel-based electrodes, *Angew. Chem. Int. Ed.* 133 (2021) 22922–22926, <https://doi.org/10.1002/ange.202110355>.
- [16] Q. Xue, H. Huang, J.Y. Zhu, Y. Zhao, F.M. Li, P. Chen, Y. Chen, Au@Rh core-shell nanowires for hydrazine electrooxidation, *Appl. Catal. B-Environ.* 278 (2020), 119269, <https://doi.org/10.1016/j.apcatb.2020.119269>.
- [17] Y. Liu, J.H. Zhang, Y.P. Li, Q.Z. Qian, Z.Y. Li, G.Q. Zhang, Realizing the synergy of interface engineering and chemical substitution for Ni<sub>3</sub>N enables its bifunctionality toward hydrazine oxidation assisted energy-saving hydrogen production, *Adv. Funct. Mater.* 31 (2021), 2103673, <https://doi.org/10.1002/adfm.202103673>.
- [18] J.Y. Zhang, H.M. Wang, Y.F. Tian, Y. Yan, Q. Xue, T. He, H.F. Liu, C.D. Wang, Y. Chen, B.Y. Xia, Anodic hydrazine oxidation assists energy-efficient hydrogen evolution over a bifunctional cobalt perselénide nanosheet electrode, *Angew. Chem. Int. Ed.* 57 (2018) 7649–7653, <https://doi.org/10.1002/anie.201803543>.
- [19] Q.Z. Qian, J.H. Zhang, J.M. Li, Y.P. Li, X. Jin, Y. Zhu, Y. Liu, Z.Y. Li, A. El-Harairy, C. Xiao, G.Q. Zhang, Y. Xie, Artificial heterointerfaces achieve delicate reaction kinetics towards hydrogen evolution and hydrazine oxidation catalysis, *Angew. Chem. Int. Ed.* 60 (2021) 5984–5993, <https://doi.org/10.1002/anie.202014362>.
- [20] Y. Liu, J.H. Zhang, Y.P. Li, Q.Z. Qian, Z.Y. Li, Y. Zhu, G.Q. Zhang, Manipulating dehydrogenation kinetics through dual-doping Co<sub>3</sub>N electrode enables highly efficient hydrazine oxidation assisting self-powered H<sub>2</sub> production, *Nat. Commun.* 11 (2020) 1853, <https://doi.org/10.1038/s41467-020-15563-8>.
- [21] H.Y. Jin, X.S. Wang, C. Tang, A. Vasileff, L.Q. Li, A. Slattery, S.Z. Qiao, Stable and highly efficient hydrogen evolution from seawater enabled by an unsaturated nickel surface nitride, *Adv. Mater.* 33 (2021), 2007508, <https://doi.org/10.1002/adma.202007508>.
- [22] A.R. Jadhav, A. Kumar, J. Lee, T. Yang, S. Na, J. Lee, Y. Luo, X. Liu, Y. Hwang, Y. Liu, H. Lee, Stable complete seawater electrolysis by using interfacial chloride ion blocking layer on catalyst surface, *J. Mater. Chem. A* 8 (2020) 24501–24514, <https://doi.org/10.1039/d0ta08543>.
- [23] H.H. Duan, D.G. Li, Y. Tang, Y. He, S.F. Ji, R.Y. Wang, H.F. Lv, P.P. Lopes, A. P. Paulikas, H.Y. Li, S.X. Mao, C.M. Wang, N.M. Markovic, J. Li, V.R. Stamenkovic, Y.D. Li, High-performance Rh<sub>2</sub>P electrocatalyst for efficient water splitting, *J. Am. Chem. Soc.* 139 (2017) 5494–5502, <https://doi.org/10.1021/jacs.7b01376>.
- [24] K. Wang, B.L. Huang, F. Lin, F. Lv, M.C. Luo, P. Zhou, Q. Liu, W.Y. Zhang, C. Yang, Y.H. Tang, Y. Yang, W. Wang, H. Wang, S.J. Guo, Wrinkled Rh<sub>2</sub>P nanosheets as superior pH-universal electrocatalysts for hydrogen evolution catalysis, *Adv. Energy Mater.* 8 (2018), 1801891, <https://doi.org/10.1002/aenm.201801891>.
- [25] Y. Zhao, N. Jia, X.R. Wu, F.M. Li, P. Chen, P.J. Jin, S.W. Yin, Y. Chen, Rhodium phosphide ultrathin nanosheets for hydrazine oxidation boosted electrochemical water splitting, *Appl. Catal. B-Environ.* 270 (2020), 118880, <https://doi.org/10.1016/j.apcatb.2020.118880>.
- [26] J.Y. Zhu, S.Q. Chen, Q. Xue, F.M. Li, H.C. Yao, L. Xu, Y. Chen, Hierarchical porous Rh nanosheets for methanol oxidation reaction, *Appl. Catal. B-Environ.* 264 (2020), 118520, <https://doi.org/10.1016/j.apcatb.2019.118520>.
- [27] J.W. Yin, J. Wang, Y.B. Ma, J.L. Yu, J.W. Zhou, Z.X. Fan, Recent advances in the controlled synthesis and catalytic applications of two-dimensional rhodium nanomaterials, *ACS Mater. Lett.* 3 (2021) 121–133, <https://doi.org/10.1021/acsmaterialslett.0c00473>.
- [28] H.J. Yu, T.Q. Zhou, Z.Q. Wang, Y. Xu, X.N. Li, L. Wang, H.J. Wang, Defect-rich porous palladium metallocene for enhanced alkaline oxygen reduction electrocatalysis, *Angew. Chem. Int. Ed.* 60 (2021) 12027–12031, <https://doi.org/10.1002/anie.202101019>.
- [29] M.C. Luo, Z.L. Zhao, Y.L. Zhang, Y.J. Sun, Y. Xing, F. Lv, Y. Yang, X. Zhang, S. Hwang, Y.N. Qin, J.Y. Ma, F. Lin, D. Su, G. Lu, S.J. Guo, PdMo bimetallic for oxygen reduction catalysis, *Nature* 574 (2019) 81–85, <https://doi.org/10.1038/s41586-019-1603-7>.
- [30] J.C. Fan, J.D. Wu, X.Q. Cui, L. Gu, Q.H. Zhang, F.Q. Meng, B.H. Lei, D.J. Singh, W. T. Zheng, Hydrogen stabilized RhPdH 2D bimetallic nanosheets for efficient alkaline hydrogen evolution, *J. Am. Chem. Soc.* 142 (2020) 3645–3651, <https://doi.org/10.1021/jacs.0c00218>.
- [31] H. Wang, W. Wang, H. Yu, Q. Mao, Y. Xu, X. Li, Z. Wang, L. Wang, Interface engineering of polyaniline-functionalized porous Pd metallocene for alkaline oxygen reduction reaction, *Appl. Catal. B-Environ.* 307 (2022), 121172, <https://doi.org/10.1016/j.apcatb.2022.121172>.
- [32] P. Prabhu, J.M. Lee, Metallocenes as functional materials in electrocatalysis, *Chem. Soc. Rev.* 50 (2021) 6700–6719, <https://doi.org/10.1039/d0cs01041c>.
- [33] L. Zhao, C.F. Xu, H.F. Su, J.H. Liang, S.C. Lin, L. Gu, X.L. Wang, M. Chen, N. F. Zheng, Single-crystalline rhodium nanosheets with atom thickness, *Adv. Sci.* 2 (2015), 1500100, <https://doi.org/10.1002/advs.201500100>.
- [34] M. Zhao, Y.N. Xia, Crystal-phase and surface-structure engineering of ruthenium nanocrystals, *Nat. Rev. Mater.* 5 (2020) 440–459, <https://doi.org/10.1038/s41578-020-0183-3>.
- [35] H.F. Cheng, N.L. Yang, Q.P. Lu, Z.C. Zhang, H. Zhang, Syntheses and properties of metal nanomaterials with novel crystal phases, *Adv. Mater.* 30 (2018), 1707189, <https://doi.org/10.1002/adma.201707189>.
- [36] Y.Y. Ge, Z.Y. Shi, C.L. Tan, Y. Chen, H.F. Cheng, Q.Y. He, H. Zhang, Two-dimensional nanomaterials with unconventional phases, *Chem* 6 (2020) 1237–1253, <https://doi.org/10.1016/j.chempr.2020.04.004>.
- [37] H.F. Cheng, N.L. Yang, X.Z. Liu, Q.B. Yun, M.H. Goh, B. Chen, X.Y. Qi, Q.P. Lu, X. P. Chen, W. Liu, L. Gu, H. Zhang, Aging amorphous/crystalline heterophase PdCu nanosheets for catalytic reactions, *Natl. Sci. Rev.* 6 (2019) 955–961, <https://doi.org/10.1093/nsr/nzw078>.
- [38] J.J. Ge, P.Q. Yin, Y. Chen, H.F. Cheng, J.W. Liu, B. Chen, C.L. Tan, P.F. Yin, H. X. Zheng, Q.Q. Li, S.M. Chen, W.J. Xu, X.Q. Wang, G. Wu, R.B. Sun, X.H. Shan, X. Hong, H. Zhang, Ultrathin amorphous/crystalline heterophase Rh and Rh alloy nanosheets as tandem catalysts for direct indole synthesis, *Adv. Mater.* 33 (2021), 2006711, <https://doi.org/10.1002/adma.202006711>.
- [39] Y.X. Zhao, C. Chang, F. Teng, Y.F. Zhao, G.B. Chen, R. Shi, G.I.N. Waterhouse, W. F. Huang, T.R. Zhang, Defect-engineered ultrathin δ-MnO<sub>2</sub> nanosheet arrays as bifunctional electrodes for efficient overall water splitting, *Adv. Energy Mater.* 7 (2017), 2006711, <https://doi.org/10.1002/aenm.201700005>.
- [40] J.F. Xie, H. Zhang, S. Li, R.X. Wang, X. Sun, M. Zhou, J.F. Zhou, X.W. Lou, Y. Xie, Defect-rich MoS<sub>2</sub> ultrathin nanosheets with additional active edge sites for enhanced electrocatalytic hydrogen evolution, *Adv. Mater.* 25 (2013) 5807–5813, <https://doi.org/10.1002/adma.201302685>.
- [41] G. Wu, X.S. Zheng, P.X. Cui, H.Y. Jiang, X.Q. Wang, Y.T. Qu, W.X. Chen, Y. Lin, H. Li, X. Han, Y.M. Hu, P.G. Liu, Q.H. Zhang, J.J. Ge, Y.C. Yao, R.B. Sun, Y. Wu, L. Gu, X. Hong, Y.D. Li, A general synthesis approach for amorphous noble metal nanosheets, *Nat. Commun.* 10 (2019) 4855, <https://doi.org/10.1038/s41467-019-12859-2>.

[42] Y. Zheng, Y. Jiao, M. Jaroniec, S.Z. Qiao, Advancing the electrochemistry of the hydrogen-evolution reaction through combining experiment and theory, *Angew. Chem. Int. Ed.* 54 (2015) 52–65, <https://doi.org/10.1002/anie.201407031>.

[43] Z.Q. Wang, X. Ren, Y.L. Luo, L. Wang, G. Cui, F.Y. Xie, H.J. Wang, Y. Xie, X.P. Sun, An ultrafine platinum–cobalt alloy decorated cobalt nanowire array with superb activity toward alkaline hydrogen evolution, *Nanoscale* 10 (2018) 12302–12307, <https://doi.org/10.1039/C8NR02071J>.

[44] C.C. Hou, Q.Q. Chen, C.J. Wang, F. Liang, Z.S. Lin, W.F. Fu, Y. Chen, Self-supported cedarlike semimetallic Cu<sub>3</sub>P nanoarrays as a 3D high-performance Janus electrode for both oxygen and hydrogen evolution under basic conditions, *ACS Appl. Mater. Interfaces* 8 (2016) 23037–23048, <https://doi.org/10.1021/acsami.6b06251>.